UC Davis
UC Davis Previously Published Works

Title
Identifying Atomic Scale Structure in Undoped/Doped Semicrystalline P3HT Using Inelastic Neutron Scattering

Authors
Harrelson, Thomas F
Cheng, Yongqiang Q
Li, Jun
et al.

Peer reviewed

Identifying Atomic Scale Structure in Undoped/Doped Semicrystalline P3HT Using Inelastic Neutron Scattering

Thomas F. Harrelson,[†] Yongqiang Q. Cheng,[‡] Jun Li,[†] Ian E. Jacobs,[¶] Anibal J. Ramirez-Cuesta,[‡] Roland Faller,[†] and Adam J. Moulé[*,†]

[†]Department of Chemical Engineering, University of California, Davis, USA

[‡]Department of Chemical and Materials Engineering, Oak Ridge National Laboratory, Oak Ridge, USA

[¶]Department of Materials Science and Engineering, University of California, Davis, USA

E-mail: amoule@ucdavis.edu

Abstract

The greatest advantage of organic materials is the ability to synthetically tune desired properties. However, structural heterogeneity often obfuscates the relationship between chemical structure and functional properties. Inelastic neutron scattering (INS) is sensitive to both local structure and chemical environment and provides atomic level details that cannot be obtained through other spectroscopic or diffraction methods. INS data is composed of a density of vibrational states with no selection rules, which means that every structural configuration is equally weighted in the spectrum. This allows the INS spectrum to be quantitatively decomposed into different structural motifs. We present INS measurements of the semiconducting polymer P3HT doped with F4TCNQ supported by density functional theory calculations to identify two dominant families of undoped crystalline structures, and one dominant doped structural

1

¹⁴ motif, in spite of considerable heterogeneity. The differences between the undoped and

¹⁵ doped structures indicate that P3HT side chains flatten upon doping.

Introduction

Recent progress in polymer based organic devices has led to significant milestones in performance, such as organic photovoltaic (OPV) power efficiencies of $>10\%$[1,2] and electron and hole mobilities >1 cm^{2}V^{-1}s^{-1}.[3,4] However, despite the successes of these materials, it is difficult to precisely identify the microstructural details that lead to desired performance. The structural and electronic details of organic electronic materials in particular are challenging to characterize and describe due to high levels of structural and electronic heterogeneity at length scales from Angstroms to micrometers.[5–8] In contrast to inorganic semiconductors, polymeric semiconductors do not follow the paradigm that increased crystalline order and repeating texture necessarily leads to improved conductivity.[9] For polymeric semiconductors, a low degree of dihedral variation can lead to highly delocalized and anisotropic charged states in materials with little or no long range crystalline order.[10]

The determination of a detailed atomic structure is challenging because the weak bonding between polymer chains in the film does not encourage long range order, allowing for many structural configurations with similar energetic minima. The lack of long range order limits the information that can be obtained from traditional structural characterization techniques such as XRD, which probes ordered domains.[11–18] Scattering techniques such as small angle neutron or X–ray scattering (SANS of SAXS) return average distance correlations but fail to determine specific geometries.[19–21] Spectroscopic techniques, such as pulsed laser experiments, can provide information about the energetic distribution of heterogeneous structures, but cannot link this distribution to any specific molecular geometry.[22–26] Even electron microscopy techniques, which can determine the location of a specific atom within a lattice to within <0.1 Å, cannot distinguish between adjacent carbon atoms (due to limited contrast),

and hydrogen atoms are invisible to most microscopy techniques.[27–29]

Analogous to inorganic semiconductors, polymeric semiconductors can be doped for a conductivity increase of up to 11 orders of magnitude.[30] However, unlike inorganic semiconductors, many polymer–dopant mixtures have low doping efficiencies, which requires increased doping ratios to achieve desired conductivity increases. Such high doping ratios cause structural rearrangements that affect the alignment of energy levels and transfer integrals, which may negatively impact the macroscopic electrical properties. For example, films of poly(3–hexylthiophene) (P3HT) and 2,3,5,6-Tetrafluoro-7,7,8,8-tetracyanoquinodimethane (F4TCNQ) have different morphologies at different doping ratios, and the conductivity does not increase predictably with dopant concentration[31–33] demonstrating the complex effect that structural rearrangement has on doping efficiency and conductivity. At high doping concentrations, F4TCNQ intercalates between P3HT chains in crystalline regions creating a new phase, which coincides with changes in the dependence of F4TCNQ concentration on conductivity.[31] Clearly, the local structure of the P3HT–F4TCNQ mixture has a large effect on electrical properties, but very little is known about the unit cell structure at atomic length scales.

In this context, we highlight inelastic neutron spectroscopy (INS) as an appropriate measurement to infer structural motifs within films of doped or undoped P3HT. Unlike electromagnetic radiation, neutrons do not interact with mobile charges present in doped materials. For this reason, the observed INS spectra only contains peaks from nuclear vibrations, and not the dielectric response of the P3HT polaron, which simplifies the comparison between doped and undoped P3HT. The INS technique hinges on resolving the time–of–flight of scattered neutrons to calculate the energy loss of the neutron after the transfer of neutron energy to a vibrational mode of the sample. The measurement provides the vibrational density of states weighted by the incoherent neutron cross section and vibrational amplitude. INS provides different information than FTIR and Raman spectroscopy because of the different atomic cross sections for neutrons and electromagnetic radiation. Scattering from all

3

hydrogen vibrations is visible using neutrons, but only vibrations that cause a change in dipole moment (such as C–H stretch vibrations) are also detectable in FTIR/Raman spectroscopy, as shown in supplemental Figures S2a,b. Those selection rules are not present in inelastic neutron scattering processes.[34] FTIR has further restrictions as the only allowed transitions must be fundamental (0–1) within the harmonic approximation. This restriction leads to sharper, better defined peaks than INS because INS allows simultaneous excitation of multiple vibrational modes, which broadens observed peaks.

To illustrate this principle, consider a system with a single high energy mode (e.g. C–H stretch), and a distribution of low energy modes (e.g. torsional vibrations between monomers). An incoming neutron may excite the high energy mode and a random low energy mode simultaneously, causing the neutron to lose energy proportional to the sum of the frequencies of the excited modes, which leads to a distribution of observable energy transfers that broadens observed peaks. An incoming photon is allowed to excite one of the modes (assuming there is a dipole), leading to a sharp, well–defined peak that presents an advantage of FTIR over INS: the peaks that are observable for FTIR are better defined than INS peaks. This concept is illustrated when considering the C–H stretch peaks observed in FTIR (SI Figure S2) versus INS (SI Figure 1). A major disadvantage of FTIR is the lack of peaks relative to INS spectra that come from bend, wag, and other complex motions, as can be seen in supplemental Figures S2b,c. Finally, electromagnetic radiation interacts with free electrons, yielding a large background signal in highly conductive samples like doped P3HT (see supplemental figure S2c). The information in an INS scattering profile can be decomposed into a linear combination of contributions from dominant structural themes. In comparison, FTIR provides structural information of the sample, but the selection rules could provide different weightings on that information from different structural configurations. As a result, an average structure can be computed from FTIR, but it is not possible to decompose the spectrum into different populations.[35] In contrast, INS provides information about the full distribution of structural configurations weighted by their density in the

[93] sample.[34] Thus, vibrational neutron spectroscopy is complementary to FTIR/Raman, but [94] also yields significant new information and is much better suited to investigate conductive [95] and heterogeneous samples.

[96] Because the INS spectrum has no selection rules and is a quantitative measurement of [97] the vibrational density of states, it can be decomposed into multiple populations. Each [98] population can then be modeled separately with high accuracy using density functional [99] theory (DFT).[36,37] Thus, the experimental spectra can be matched to a combination of [100] proposed structures whose spectral contributions are determined from DFT. In addition, [101] the charge distribution calculated using the DFT model can be constrained by fitting to the [102] measured data, which has numerous modes. In this way, the structure of the configuration [103] in the sample is inferred from the dynamics of the atoms in the film, which is dependent on [104] the charge distribution. Configurations that do not adequately represent the experimental [105] INS spectra can be summarily removed.

[106] Previously, INS has been used to study the vibrational dynamics and structure of poly- [107] mers. Early studies used INS to understand the low frequency dynamics of poly–acetylene,[38] [108] polyaniline,[39] and PPV[40] demonstrating that INS provides valuable low–energy dynamic in- [109] formation for conjugated polymers that could be important for understanding charge trans- [110] port. However, the short range dynamic information was missing from the spectra due to the [111] low neutron flux and small energy range of early INS instruments; instrument resolution de- [112] creased with increasing energy transfers, meaning that short range dynamic information was [113] missing from the spectra. Current INS spectrometers, including VISION at the Spallation [114] Neutron Source,[41,42] TOSCA at the ISIS laboratory,[43] and LAGRANGE at the Institute [115] Laue–Langevin,[44] are capable of providing high–resolution spectra across the entire vibra- [116] tional energy range (5 meV – 1 eV). Thus, these spectrometers can observe long–range, [117] low energy lattice dynamics, and high–energy, short range bond vibrations simultaneously. [118] With these high–resolution instruments, the local structure of polymers has been inferred [119] from INS spectra because the vibrational modes sensitively depend on the spatial arrange-

ment of neighboring atoms/molecules. For instance, the TOSCA spectrometer was used to identify the zig–zag structure of PEO under confinement,[45] as well as the local structure of adsorbed hydrogen on a nickel catalyst.[46] On the other hand, the VISION spectrometer was recently used to identify the complex structure of highly disordered kerogen[47] demonstrating that high–resolution INS is capable of providing structural as well as dynamic information. Hermet et al. demonstrated that INS can also be used to identify the presence of different crystalline polymorphs of quaterthiophene and sexithiophene.[48]
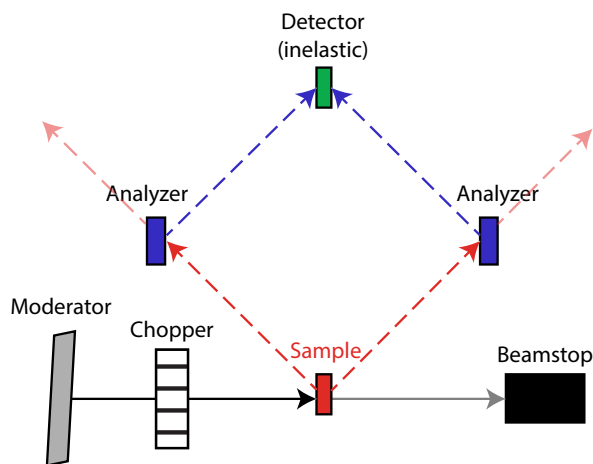

Figure 1: *Schematic representation of the VISION spectrometer. The analyzers determine the final neutron energies, which are used to find the amount of energy transferred to the sample by recording and analyzing the time of flight of the neutrons from each pulse.*

Our study builds on prior studies by demonstrating that INS can be used to study the structure of both doped and undoped disordered organic electronic materials. We demonstrate here that the distribution of configurations contained in heterogeneous films of doped and undoped P3HT can be resolved into contributions from dominant structural motifs that we can identify using the VISION spectrometer and DFT. We decompose the undoped spectrum into contributions from the crystalline and amorphous regions to find three key structural motifs in the film, one in the amorphous region, two in the crystalline region. We also find a dominant structural motif of a P3HT film that has been heavily doped by F4TCNQ, producing a crystal structure of P3HT with intercalated F4TCNQ that agrees

6

with both theory and experiment.

Materials and Methods

Materials

Regioregular P3HT (>98%, $M_n = 54 - 75$ kDa), regiorandom P3HT and F4TCNQ ($\geq 97\%$) were purchased from Sigma–Aldrich. Undoped samples were used as received by the manufacturer in INS experiments unless otherwise indicated. For the doped samples, P3HT and F4TCNQ were first dissolved in chloroform. Solutions were then mixed in appropriate ratios to achieve the desired doping levels, and the solvent was evaporated inside a nitrogen glovebox at low temperature over several days. The solids were chopped into a powder (500 mg for each sample) using a razor blade and loaded into rectangular aluminum sample holders and sealed for measurement.

Inelastic Neutron Scattering

We used the VISION spectrometer at the Spallation Neutron Source at Oak Ridge National Laboratory (Figure 1) to characterize the ensemble of structural configurations present in our doped and undoped P3HT samples. The VISION spectrometer is ideally suited for inferring structural information from polymer films. Figure 1 shows the experimental setup of the VISION spectrometer. The analyzers and the Be filters select the final neutron energy loss. Time–of–flight analysis allows for computation of the energy spectrum transferred from the incident white beam of neutrons to the polymer film. The experimental set up improves the count rate and signal to noise ratio over other INS instruments by over two orders of magnitude, allowing rapid acquisition of full spectrum data.[41] To minimize the Debye–Waller effect, which causes broadening of the spectral information due to random fluctuations of the atomic position, the scans were performed at 5 K. This low temperature provides the level of detail required to probe sensitive structural changes during doping. It is possible

7

that the low temperature of the measurement could induce crystalline phase transformation. However, we do not expect major morphological changes in P3HT, because main chain and side chain melting occurs at $\sim 200^oC$ and $\sim 50^oC$, respectively.[49,50] In addition, Poelking et al used molecular dynamics to show that polymorph I' does not reform from polymorph I after cooling.[51] Large scale reorganization would require mobile main chains and/or side chains, which is unlikely as the temperature is lowered. Nevertheless, it remains possible that temperature–induced structural reorganization is taking place.

Computational Methods

We used plane–wave density functional theory with norm–conserving pseudopotentials and the PBE functional[52,53] to calculate the optimized structures within the CASTEP framework.[54] PBE is a common choice for understanding the structure of molecular crystals, including quaterthiophene and sexithiophene, which are chemically similar to P3HT.[48,55,56] Density functional perturbation theory (DFPT) was used to calculate the phonon spectrum of the optimized structures instead of finite difference methods because DFPT allows computation of vibrational modes at multiple k–points whereas the finite difference method is restricted to the gamma point only. The initial structures for the simulations were created within the Materials Studio® suite. The lattice parameters were determined from published X–ray diffraction,[31] and molecular dynamics studies.[51] The atomic coordinates were relaxed so that the maximum interatomic force was below 0.01 eV/Å. We used a 2 x 3 x 3 and a 1 x 2 x 2 k–point sampling grid to simulate the undoped and doped configurations, respectively. More k–points were used to sample longer dimensions in the Brillouin zone (smaller real space lattice dimensions). We used aCLIMAX 6.0[57] to convert the finished phonon calculations to INS spectra that can be compared to experiments. The details of the conversion from vibrational modes to an INS spectrum are found elsewhere.[34,57] All simulated frequencies were scaled by a constant factor (1.015 in this study) to better agree with the experiments. The use of a scaling factor has been used in many prior DFT studies to replicate experimental

8

[186] vibrational modes.[46,58,59]

[187] Since the initial geometries were relaxed prior to calculating vibrational frequencies, the [188] relaxed configuration commonly differed greatly from the initial geometry, which led to [189] problems with using experimental unit cells as starting points. We altered the dihedral [190] angles of the first bond of the side chain, and the displacement of thiophene rings in the [191] direction of the backbone until we achieved a relaxed geometry that matched configurations [192] determined from X–ray data.

[193] We iteratively adjusted parameters such as the dihedral angles between thiophene rings, [194] the dihedral angle of the first bond of the side chain and the displacement of one chain [195] relative to another chain to generate a set of configurations likely to represent the data [196] and consistent with previously published crystallographic data. Likely configurations were [197] chosen because the associated simulated spectra showed peaks at the correct frequencies [198] compared to experimental data. This means that only configurations that were matched to [199] both published crystallographic and our INS data are presented.

Results and Discussion

INS Experimental Data

[202] Regio–regular P3HT is a semicrystalline polymer that forms films with 20–50% crystalline [203] and 50–80% amorphous phase fractions.[9,50,60] The molecular structures of P3HT and F4TCNQ [204] are shown in Figure 2b,e. When F4TCNQ comes into contact with an electron donor, like [205] P3HT, charge transfer to F4TCNQ results in a positive charge that is delocalized along [206] the polymer backbone which changes a large number of molecular vibrations visible to high [207] resolution INS. In addition, the crystalline portion of P3HT has been reported to show sig- [208] nificant paracrystallinity, which means that the individual monomers experience significant [209] structural heterogeneity even within crystalline domains.[9,51] The total structural heterogene- [210] ity is expressed in the INS spectrum as a weighted sum of all different contributions, which
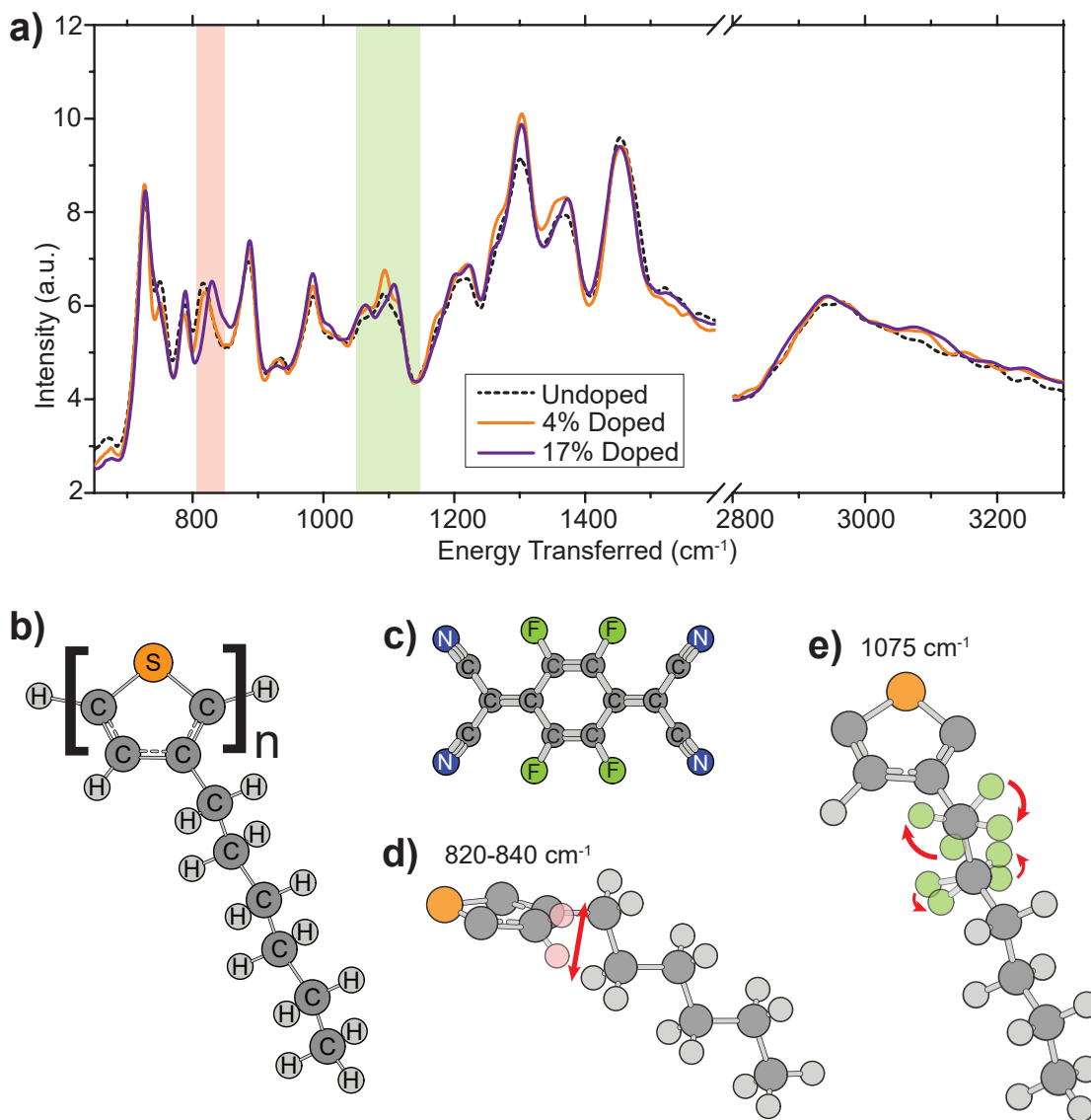
9

Figure 2: *a) Experimental INS spectrum from $650 - 3300$ cm⁻¹ of undoped P3HT, P3HT doped with 4 mol% F4TCNQ, and P3HT doped with 17 mol% F4TCNQ. The highlighted regions correspond to vibrational modes depicted in d,e. b,c) Molecular structures of P3HT and F4TCNQ. d,e) Vibrational modes that are most sensitive to doping from F4TCNQ. We show an out of plane bending mode of the backbone hydrogen at $820 - 840$ cm⁻¹ (d), and a torsion between the first and second side chain carbons at 1075 cm⁻¹ (e).*

211 leads to peak width (along with dispersion and phonon wings) and even the presence of sev-

212 eral different peaks originating from identical motions in differing molecular environments

213 (for example in crystalline and amorphous domains).

214 The vibrational spectra in Figure 2a represent samples of undoped, 4 mol% doped, and

17 mol% doped regio–regular P3HT with F4TCNQ. The spectra were normalized to equal background intensity. These doping levels were chosen because 17 mol% doping was reported to be the highest possible doping level (without formation of a pure F4TCNQ phase) for P3HT by F4TCNQ.[31] Doping at 4 mol% represents a lightly doped material in which most of the F4TCNQ is expected to reside in the amorphous domains of the polymer.[31,33]

Each peak corresponds to a vibrational transition that occurs when an incident neutron interacts with the nuclei in the sample. The peak height is proportional to the amplitude of the vibrational motion, and the energy of each transition reflects the frequency of the vibrational mode. Changes in energy of the same peak in different samples stem from changes in inter–atomic forces causing a particular mode to either stiffen (shift to higher energy) or relax (shift to lower energy). The changes in the height and frequency of a given peak may come from compositional changes to the ensemble of configurations present, as well as the reasons provided above. We model the data using DFT well enough to assign these peaks to particular vibrational modes, which agrees with prior studies.[49] We highlight two peaks, denoted by shaded regions in Figure 2a, most affected by doping, corresponding to the two vibrational modes in Figure 2d,e. The peaks are associated with the out of plane (OOP) bending of the backbone hydrogen, and the torsional bending of the first/second carbons in the side chain occur at ∼820–840 cm^{-1}, and ∼1075 cm^{-1}, respectively.

The OOP bending mode of the backbone hydrogen stiffens when heavily doped. The 17 mol% doped sample displays a blue shift in this peak compared to the 4 mol% doped and undoped P3HT spectra. This blue shift is likely due to the intercalation of F4TCNQ into the crystalline regions at high doping ratios, in which the reduced distance between F4TCNQ and P3HT increases the intermolecular forces acting on the OOP mode. At 4 mol% doping ratio, F4TCNQ primarily remains in the amorphous regions of the polymer. Two prior studies and the lack of blue shift in the OOP bending peak corroborate this assignment.[31,33]

The torsional vibrations of the first and second carbons of the side chain are very sensitive to the torsional angle between the side chain and backbone of P3HT. Using DFT (discussed
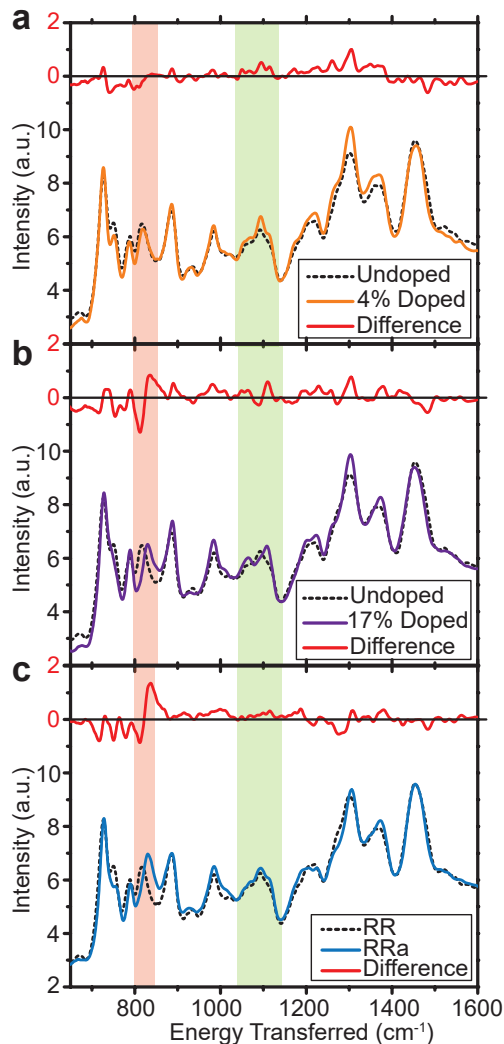
11

Figure 3: *a) The regio–regular (RR) undoped and 4 mol% RR–doped spectra are compared between 650–1600 cm^{-1}. The red curve corresponds to the difference between the 4 mol% doped curve and the undoped curve. b) The RR–undoped and 17 mol% RR–doped spectra are compared between 650–1600 cm^{-1}. The red curve is the difference between the 17 mol% doped curve and the undoped curve. c) The RR–undoped and regiorandom (RRa) undoped spectrum are compared between 650–1600 cm^{-1}. The highlighted regions correspond to vibrational modes depicted in Figure 2. The red curves above the spectra in a–c are the differences between the spectra.*

later), we see that the change in torsional angle causes two overlapping peaks at 1075 cm^{-1} to shift to higher and lower energies at high doping levels. The shift occurs as a larger proportion of P3HT configurations contain side chains in the plane of the backbone as we will show below. The flattening of side chains agrees with X–ray diffraction showing an

246 increase in the long axis of the unit cell upon doping.[31] Our DFT results also show that 247 when a P3HT side chain is flat with respect to its backbone, the torsional mode blue shifts, 248 and a coupled carbon-carbon stretching mode along the length of the side chain slightly 249 increases in amplitude causing an increase in intensity (see the Supplementary Information 250 for a visualization of the modes).

251 The spectrum also shows that the peak at $1300\ \mathrm{cm}^{-1}$ increases in amplitude when compar- 252 ing undoped and 4% doped. Using our DFT results, we assigned this peak as a combination 253 of many twisting modes of the side chain hydrogens. The increase in peak height could be due 254 to a combination of many factors. In general, changes in peak height are due to changes in 255 vibrational amplitude and/or compositional changes in the polymer. Compositional changes 256 include local configurational changes, and changes in the amorphous/crystalline volume 257 fractions. Doping P3HT results in a charged backbone, which could cause configurational 258 changes, and changes in intramolecular forces, both of which can affect the vibrational mode 259 energies and amplitudes. It seems that this peak is unaffected by changes in amorphous 260 volume fraction because this peak does not show a change in height when comparing un- 261 doped RRa and RR P3HT. In addition, prior X-ray studies show only a small amount of 262 structural reorganization when comparing undoped and 4% doped, so it would make sense 263 that charging the backbone is responsible for the increase in peak height (either through 264 changes in local configuration or increase in vibrational amplitude). However, we cannot 265 make any conclusions about the cause of the increase in this peak's height at this time.

266 Figure 3 shows the compositional dependence of the INS spectra. The spectral differences 267 between undoped and 17% doped are clearly shown in Figure 3b, where the OOP bending 268 peak shifts to higher energy, and the overlapping modes in the green region shift into two 269 distinct peaks. In contrast, Figure 3a shows almost no spectral differences between undoped 270 and 4% doped samples. The difference curves in Figure 3a,b reinforce the contrast between 271 the two doping levels. A doping ratio of 4 mol% does not affect the vibrational structure as 272 much as a doping ratio of 17 mol%, demonstrating that the local structure is changed most

13

in a heavily doped sample.

The spectra in Figure 3 represent samples that have both amorphous and crystalline phases, which convolute our interpretation of the spectra because we can't explicitly attribute a spectral change between samples to a change in intermolecular forces (small scale) versus a change in phase volume fractions (large scale) because doping likely changes the crystalline phase fraction. Thus, we need a sample with a single phase to distinguish between crystalline and amorphous configurations. Regio–random (RRa) P3HT has an identical chemical structure to regio–regular (RR) P3HT, however the hexyl side chain is randomly attached to either the second or third carbon of the thiophene ring, which generates films that do not show an X–ray crystal structure and therefore are uniformly amorphous.[61–63] Thus, we can study the vibrational structure of the amorphous region independently, assuming that the random change in side chain attachment does not strongly affect the vibrational modes of the polymer.

Figure 3c shows a comparison of the INS spectra of undoped RR–P3HT and RRa–P3HT, with the difference between the spectra plotted above. This comparison demonstrates the vibrational difference between a composite amorphous/crystalline system (RR–P3HT), and a uniformly amorphous system (RRa–P3HT). The OOP bending region at 820–840 cm^{-1} is the only peak with a vibrational frequency that is strongly affected by the change in phase composition, indicating that the OOP bending mode is relaxed by more delocalized electronic states present in crystalline regions of polymer chains. Electronic delocalization is a result of decreased dihedral angle variation between backbone monomers.

Simulation of Crystalline Domains

Plane wave density functional theory is the best approach to model the INS data as it allows the accurate prediction of vibrational modes in crystalline samples. The periodicity implicit in using a plane wave basis set allows the simulations to model extended solids, which provides the intermolecular interactions absent in typical gas phase DFT simulations.
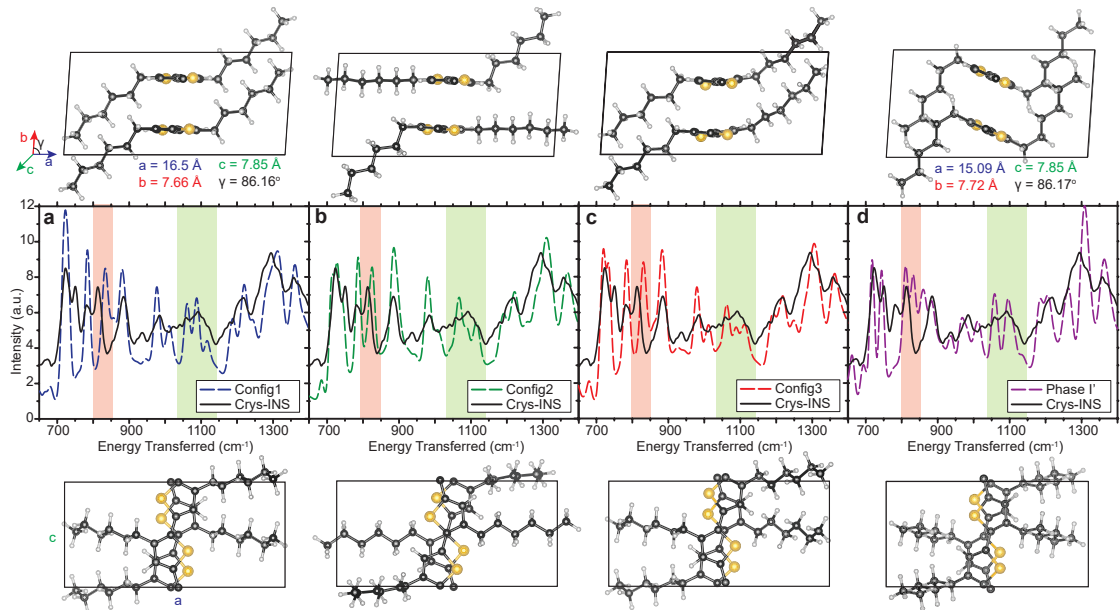
14

Figure 4: *Simulations of three different potential P3HT crystalline configurations (Config1(a), Config2(b), Config3(c), and Phase I'(d)). In all cases, the simulated spectrum is plotted against the experimental INS spectrum of undoped P3HT between 650–1400 cm⁻¹. The side view (top row) and top view (bottom row) of each configuration is shown.*

Semicrystalline P3HT has ∼40–50% crystalline domains by volume,[9] indicating that a significant portion of P3HT can be described by plane–wave DFT, but long-range structural correlations will be overestimated. To correct these errors, we would need to simulate large unit cells to account for the proper decay in structural order. However, the computational expense of DFT limits the size of the unit cell, meaning long range curvature present in real polymer systems cannot be modeled. We are assuming that the curvature effects on the spectrum are small compared to changes in local (∼10 Å) structure, which is reasonable provided that we only simulate modes that are sufficiently high in energy (i.e. > 700 cm⁻¹). In this energy range, we expect that the local ordering of adjacent polymers will be the dominant perturbation to the vibrational modes.

Semicrystalline P3HT contains several different crystalline polymorphs which have been identified from X–ray measurements.[15,17,18,51,64] The most thermodynamically favorable polymorph is Phase I as determined by Poelking et al using a molecular dynamics approach. We

15

also consider the Phase I' polymorph proposed by Poelking et. al.,[51] but do not consider other polymorphs, such as Phase II because Phase II is irreversibly transformed into Phase I at room temperature and requires specific sample preparation that we did not apply.[65,66] The assumed structure of Phase I P3HT has the backbone plane parallel to the top/bottom face of the unit cell and side chains are tilted at an angle of approximately 47° with respect to the backbone plane.[17,51,64,67] Phase I' P3HT is energetically favored at low temperatures.[51] In the structure of Phase I', the backbone plane is tilted with respected to the top/bottom face of the unit cell, and the angle between the side chains and the backbone is approximately 79° relative to the plane of the backbones.

RR–P3HT films are composed of amorphous and crystalline regions. We can generate an approximation for the crystalline region spectrum if we assume that the RRa–P3HT spectrum describes the amorphous regions of P3HT perfectly. Here we assume that the experimental spectrum is comprised of a combination of independent amorphous and crystalline spectra, and we can assume that the amorphous phase comprises 55 vol% based on the work of Noriega et al.[9] The crystal INS spectrum is calculated as the total RR–P3HT spectrum minus the RRa–P3HT spectrum multiplied by its volume fraction. Here, we must assume that RRa–P3HT has the same INS spectrum as 100% amorphous RR–P3HT. To support this assumption, we highlight the recent work of Shen et al, in which they demonstrated that the amorphous phase of RR–P3HT contains locally ordered sections of polymer likely due to interfacial regions between crystalline and amorphous domains, and that RRa–P3HT contains locally ordered regions as well due to assembly of local regio–regular segments.[68] Due to the structural similarities between RR and RRa P3HT, Shen et al subtracted GI–WAXS spectra of RRa–P3HT from RR–P3HT to find the crystalline volume fraction of RR–P3HT, which agrees with the results by Noriega et al.[9] Based on these results, we can directly compare the results of plane–wave DFT simulations to the crystalline INS spectrum to isolate structural motifs likely present in semicrystalline P3HT.

Simulations of an infinite crystal of Phase I P3HT (referred to as Config1) with identical

side chain configurations show a poor fit to INS data (Figure 4a). We therefore introduce heterogeneity in the crystalline phase of P3HT by simulating multiple side chain angles (Config2) and dihedral disorder (Config3), while maintaining the same unit cell, which improved the fits (Figure 4b and 4c). Differences between measured and modeled data are primarily visible in the wag and bend vibrations between 650–1400 cm^{-1}. The entire simulated spectrum can be found in Supplementary Information Figure S3 and S4. The simulated spectrum for Config1 shows the largest error (from a least squares regression) with the measured INS data in the OOP bending region (red shaded region in Fig 4), indicating that this stacking motif likely represents only a small fraction of undoped P3HT. The best fit (largest fraction) for the backbone hydrogen OOP bending mode is displayed by Config2 (Figure 4b). This indicates that the OOP bending mode of the backbone hydrogen is coupled to the dihedral angle of the first carbon on the side chain, as seen in the INS spectrum. In Config2, each side chain alternates between a bent and flat dihedral angle with respect to the backbone plane. This side chain alternation leads to a 0.502 Å offset between P3HT backbones along the a–direction of the unit cell. For Config3 (Figure 4c), the dihedral angle between adjacent backbone monomers was adjusted to induce a slight twist along the backbone, which captures the uncertainty in the monomer-monomer dihedral angle seen in prior molecular dynamics studies.[51,69] This twist creates a simulated spectrum that is between Config1 and Config2 in quality of fit. Config2 and Config3 both show a slight splitting/broadening of the peak at 750 cm^{-1} (representative of torsional vibrations of side chain hydrogens), which is completely absent from the spectrum of Config1, but consistent with the measured INS data.

The choice of alternating flat and angled side chains within the unit cell of Config2 may seem arbitrary, but was chosen to favorably pack flat side chains into an experimentally verified unit cell. A configuration with completely flat side chains require a longer unit cell along the a axis. Extending one side chain (out of four) to the flat configuration results in unstable steric interactions between the flat side chain and the angled side chain in the

17

adjacent unit cell. Incorporating two flat side chains allows the polymers to nicely pack into an appropriately sized unit cell. Certainly one could imagine additional configurations that fit into the unit cell (by twisting dihedral number 2–5 along the side chain), but properly sampling of these configurations is computationally infeasible. In addition, we do not expect that configurational variations to the side chain will have a strong effect on the OOP and torsional vibrations. Nevertheless, it is important to stress that each of the configurations presented in Figure 4 are representative of different structural families/motifs.

The flat side chain motif in Config2 shows two distinct peaks in the torsional region of the spectrum (green shading). The presence of these two peaks does not agree with the measured INS data. The highest peak in the highlighted green region is due to a coupled carbon–carbon stretching mode that is amplified due to the completely flat side chain. Peak intensities in the region between 1050–1200 cm^{-1} are better described by Config1. The fact that Config1 fits better in the torsional (green shading) region of the spectrum and Config2 fits better in the OOP bending (red shading) shows that the experimental spectrum can not be explained using a single molecular configuration. Instead, this analysis indicates that there are multiple different configurations present in the sample.

We also tested whether the proposed Phase I' crystalline structure of P3HT was consistent with the measured INS spectrum (Figure 4d). The Phase I' structure has been measured and discussed as an energetically but not entropically favorable structure, meaning that it could be dominant with some thermal processing and would be stable at low temperatures like those used for the INS measurements.[51] Recent studies (both experimental and computational[15,18,51,69]) predict the presence of P3HT configurations with tilted backbone planes with respect to the top/bottom faces of the unit cell, demonstrating that the configuration of P3HT inside the unit cell is still disputed. The simulated spectrum of Phase I' P3HT fits to the crystalline spectrum better (lower sum of squared error) than Config1, but less well than Config2 and Config3. However, the spectrum for Phase I' does have a prominent double peak near 700 cm^{-1}, which is mostly absent from the configurations present in Fig-

ure 4, indicating that Phase I' may be present as a fraction of the total volume. Since INS allows the superposition of spectral contributions of different configurations that sum to the total observed spectrum, a linear superposition of the four crystalline, simulated spectra is appropriate to determine phase fractions in crystalline domains.

Linear Combinations of Spectra

The semicrystalline nature of RR–P3HT requires a linear combination of spectral contributions from different configurations and/or phases. Conveniently, the INS data can be decomposed into contributions from different configurations whose weights represent specific volume fractions of the particular configurations and/or phases because INS is a technique that equally weights the contribution from every vibrational mode (no selection rules).
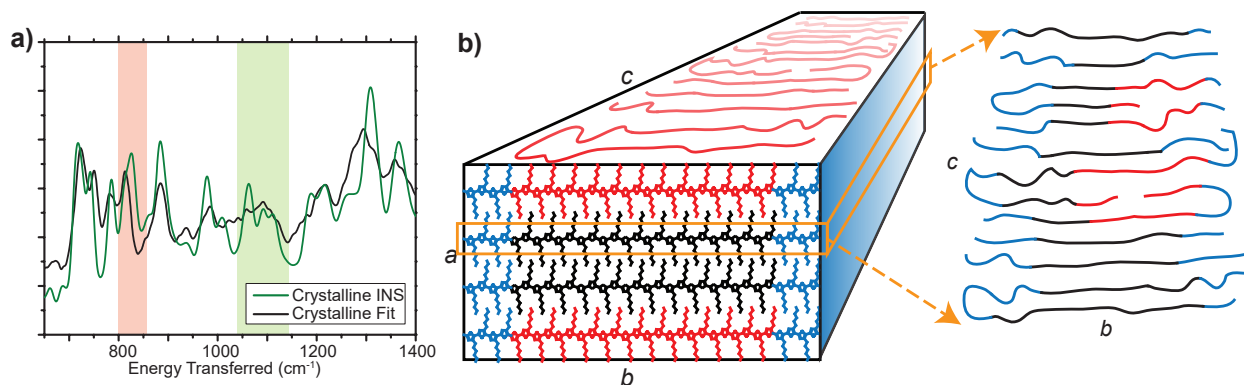

Figure 5: *(a) Fitted linear combination of simulated spectra plotted against the experimental INS spectra (generated by subtracting the amorphous (RRa) fraction from the total undoped spectrum). (b) Cartoon of crystalline region of P3HT where black, red, and blue regions represent different configurations.*

Table 1: Linear Combination Weights

System	Config1	Config2	Config3	Phase I'
Crystalline	0%	60%	2%	38%

The weights of the optimal linear combination of effective crystalline spectrum

(defined in text) to 4 crystalline configurations.

19

Using the previously discussed crystalline INS spectrum, we combine the four crystalline DFT simulations to find the optimal linear combination of structural motifs. Figure 5a represents a least squares fit of the four crystalline simulations to the crystalline experimental spectrum. The contribution of each simulation is given by Table 1 indicating that the dominant structural motif is Config2 (60%), followed by Phase I' (38%) and Config3 (2%). The error of the least–squares fit depends on the accuracy of the instrument and the computational method. As the experimental uncertainty within the energy transfer window discussed (600–1400 cm^{-1}) is quite low, the majority of the error lies with the assumptions and convergence criteria (very tight convergence criteria was used) of DFT. Thus, these proportions are the linear combination fit of the four crystalline structures is correct within the accuracy given by the PBE functional. However, as mentioned before, these structures are representative of different structural motifs. We expect more side chain heterogeneity in a real system, which would produce broader peaks in the non–highlighted regions of Figure 5a. Thus, the structural proportions presented in Table 1 only approximately correlate to the true proportions of structural families in the real material. Despite the approximate nature of our results, we can still draw conclusions from the fit between the four representative configurations.

There is no contribution from Config1, the most often cited crystalline motif from X–ray diffraction measurements. The high percentage contribution from Phase I' is due to the presence of a second peak around 750 cm^{-1}, and absence of a peak at 775 cm^{-1}. The other configurations do not display a peak at 750 cm^{-1}, and overestimate the height of the peak at 775 cm^{-1}. Thus the combination of Phase I' and Config2 synergistically describes the experimental data. The ratio of Config2 and Phase I' contributions to the fit of the INS data is fairly consistent in both the crystalline only fit and to the fit of the unaltered RR–P3HT spectrum (see Supplementary Information). This indicates in particular that there are a variety of side chain angles with respect to the backbone in crystalline P3HT domains and that the angle of the backbone with respect to the unit cell is not constant. We

20

again point out that P3HT forms crystalline ribbons and the crystalline chains in the center of the ribbon may have significantly different geometry due to the presence of an ordered crystal field compared to P3HT that forms the top, bottom, internal domain boundaries, and ribbon edges (Figure 5b). In addition, real morphologies likely contain continuous transitions between crystalline and amorphous regions, which should increase the structural heterogeneity, overall peak width, and background of our simulated spectrum.

The question of whether or not the backbone is tilted with respect to the top/bottom face of the unit cell has long been disputed.[18,51,67] Our results demonstrate that both stacking motifs are present in the crystalline region, and can be elucidated with INS, emphasizing the sensitivity of this measurement technique. Poelking et al used molecular dynamics to show that the crystalline phase had thiophene rings that were flat with respect to the top/bottom of the unit cell,[51] whereas a similar study using a different force field showed that similarly sized polymer chains (20–mers) generate a unit cell with a tilted backbone.[69] This discrepancy highlights the theoretical difficulty in identifying the local atomic–level structure. In the latter study, the backbones changed from a tilted configuration to a flat configuration when the chain length was increased to 40–mers, suggesting that the crystalline phase may contain regions with both tilted and flat backbones.

Our results help rationalize the differences observed in prior molecular dynamics[51,69] and experimental studies[15,18,64,67] considering the picture of the crystalline domain in Figure 5a. The INS data suggests that the crystalline domain is comprised of at least three distinct structural motifs, which can be explained by three different local field regimes within the crystalline domain that cause changes in local structure of the polymer. The inner region of the crystalline domain is different from the regions at the top/bottom and left/right of the domain (Figure 5a), which may cause distortions in the side chain tilt and/or dihedral angle between monomers. We can postulate that the blue, red, and black segments of Figure 5a correspond to dihedral distortions (Config3), side chain tilt variation (Config2), and a highly crystalline morphology (Phase I'), respectively. While this postulate intuitively makes sense,

21

we cannot assign the colored segments of Figure 5a to specific configurations presented in this study without a larger length scale model. However, we can conclude that the crystalline domain of P3HT is structurally heterogeneous at the atomic level with three local structural motifs dominating the distribution of configurations.

Doped Simulations

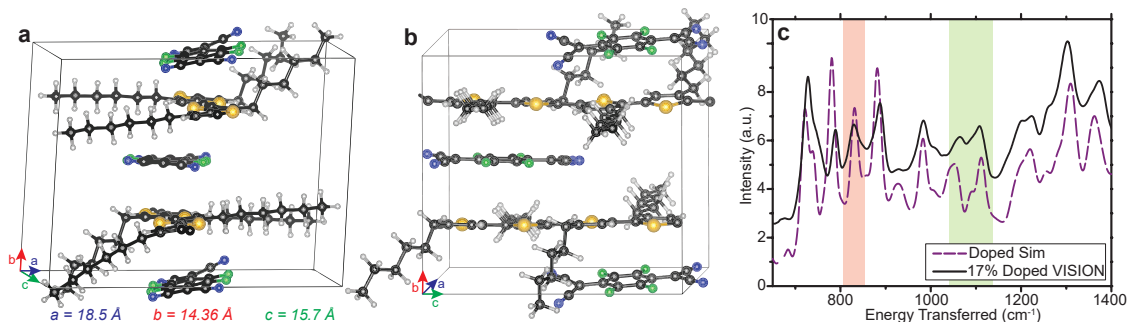Figure 6: *(a) Front view, and side view (b) of structure of doped P3HT in the crystalline phase used for simulation. b) The simulated spectrum is plotted against the 17 mol% doped INS spectrum.*

Recent publications about P3HT doped with F4TCNQ[31,33] clearly show that at low doping ratios (≤3 mol%), F4TCNQ is mostly found in amorphous domains. At higher doping ratios, F4TCNQ inserts between P3HT backbone planes. Although at 4% doping some F4TCNQ likely does intercalate, this does not have a significant effect on the vibrational spectrum, as seen in Figure 3. The maximum doping ratio is approximately 17 mol% and represents full intercalation of F4TCNQ into crystalline domains in addition to doping of the amorphous sections of the polymer.[31,70] The 17 mol% doped sample represents a much more uniform sample than lower doping ratios because doping likely causes planarization of the P3HT backbone, which removes local structural heterogeneity.

Figure 6 shows a fit to the INS spectrum of P3HT doped with 17 mol% F4TCNQ that represents a dominant configuration. Since we do not know the volume of amorphous domains in the doped polymer, the peak heights are difficult to quantitatively explain, so we

will focus on the peak energies. The simulated spectrum shows good agreement with the doped experimental spectrum for all vibrational peak frequencies. This indicates that the structure presented in Figure 6a is dominant in the doped ensemble. Both highlighted regions are well explained by the simulation showing that the stacking motifs present in the structure are widespread throughout the system. F4TCNQ is intercalated between P3HT chains, but not adjacent to the same monomers; one is displaced along the c axis relative to the other. The lattice constants were taken from a combination of X–ray diffraction[31] and molecular dynamics studies.[51] The plane of the backbone (created by the flat face of the 5–membered thiophene ring) is parallel to the plane of the closest dopant. The two chains are not vertically aligned with one another, indicating that F4TCNQ prefers to interact with a single P3HT chain. The molecular planes of the dopants are not parallel, causing both P3HT chains to distort and twist along the backbone indicating that charging the backbone/F4TCNQ combination may cause some puckering/distortions in the backbone to minimize the electrostatic potential. The average charge transfer between P3HT and F4TCNQ in this configuration is 0.92 electrons from the P3HT to F4TCNQ using Mulliken analysis.[71,72] This near integer charge transfer from P3HT to F4TCNQ is consistent with spectroscopic analysis.[73]

The INS data shows strong interactions in the OOP bending and torsional modes, which involves hydrogens on the backbone and the first and second carbon of the side chain. In our simulated structure, we see that some of the nitrogen/fluorine groups are nearest to either the backbone hydrogen or the hydrogens attached to the first carbon of the side chain. The electronegative atoms are close enough to interact with the hydrogens responsible for the OOP bending and torsional bending modes but not close enough to call these hydrogen bonds. These dipolar interactions, in addition to the electrostatic attraction of the negatively charged dopant to the positively charged polymer, have a strong effect on the determination of the dopant location with respect to the polymer. The fact that the simulated spectrum matches at every vibrational peak in these regions is a strong indication that the proposed

23

structure is valid. In addition, each peak in the displayed energy range is well explained by a single configuration. Since we required two major configurations to explain the undoped spectrum, we can infer that the distribution of local configurations shrinks when heavily doped. In other words, there appears to be more local order when P3HT is heavily doped.
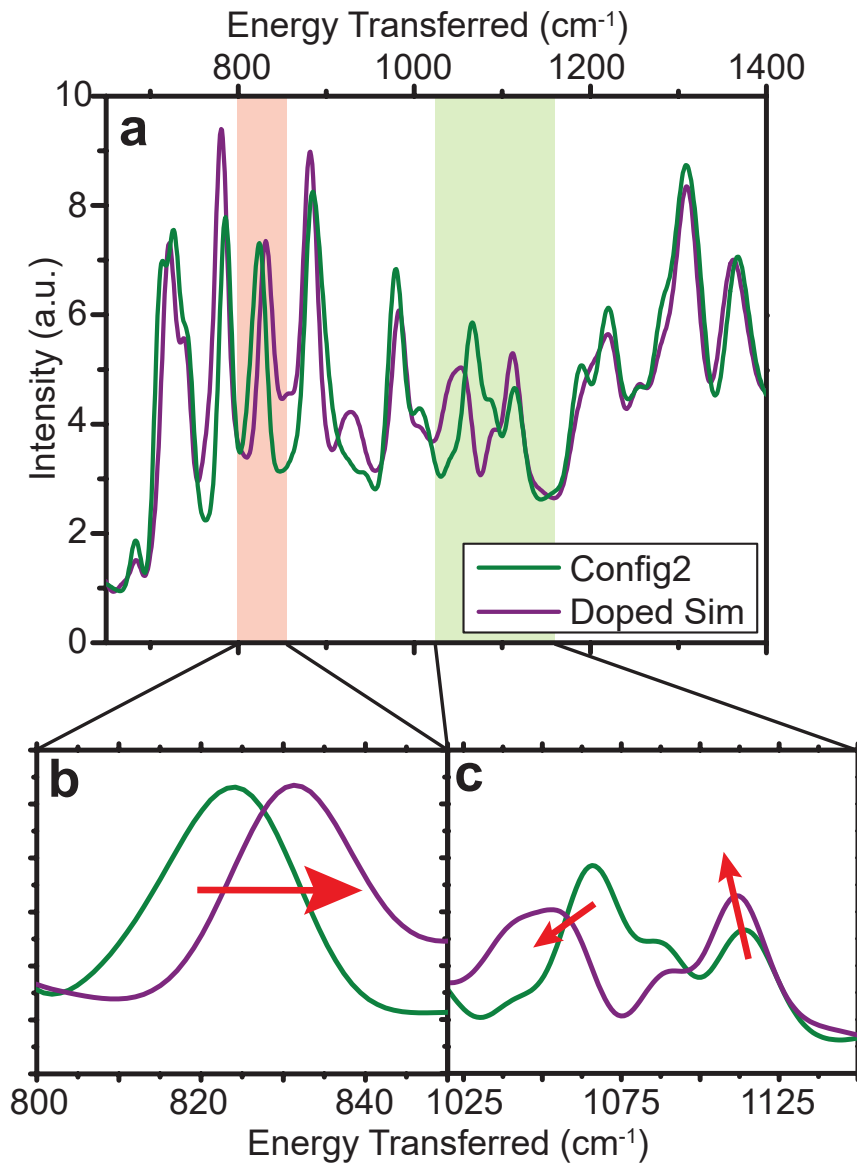

Figure 7: *The simulated spectra of Config2 and the doped configuration are compared. The two shaded regions are expanded to demonstrate the specific effect of doping.*

The simulated spectra of undoped Config2 and the simulated doped configuration are compared to demonstrate the internal consistency of the modeling approach. Config2 was

chosen because it is the undoped configuration most similar to the doped configuration, and the most prevalent configuration in the undoped crystal. The OOP bending peak at $\sim$820 cm^{-1} blue shifts upon doping as seen in the experimental spectra (Figure 7b). This blue shift is likely due to a combination of increased electrostatic interactions between dopant and backbone hydrogen and/or charging of the backbone (through doping) leading to a stiffer mode. F4TCNQ is 3.59 Å away from the P3HT backbone, whereas the P3HT chains are 3.83 Å away from each other when undoped, which reduces the average interaction distance of the backbone hydrogen. As a result, the backbone hydrogen experiences greater forces when moving perpendicular to the plane of the backbone.

The doped simulation displays a greater splitting between peaks in the torsional region of the spectrum (Figure 7). The peak at $\sim$1120 cm^{-1} increases in amplitude, while the peak at $\sim$1065 cm^{-1} shifts to lower energy upon doping. The former is due to a red shift (lower energy) in an in–phase, coupled rowing vibration of hydrogens along a flat side chain (see Supplemental Information Figure S9d). When P3HT is doped, this motion has a similar energy to the torsional vibration as shown in Figure 2c, causing the increase in peak height. The shift in the peak at 1065 cm^{-1} to lower energy is the result of a relaxation of coupled carbon-carbon stretching modes along the length of the side chains. The motion of the side chain carbons and hydrogens close to the backbone are less stiff when doped. The positive charge on the backbone, coupled with the electron donating nature of the hexyl side chain, make the side chain bonds less stiff. All of these simulated vibrational changes due to doping are consistent with the trends observed in the experimental spectra.

Conclusions

The INS instrument VISION records a spectrum that is similar to the pure density of vibrational states, which means that the data is a superposition of the amplitude and frequency for each vibrational mode for each configuration of P3HT. By investigating the major trends

25

in amplitude and frequency for several indicator modes, we are able to ascertain configurations of P3HT that are the most prevalent structural themes. Specifically, we demonstrate that the crystalline configurational distribution contains at least three dominant structural motifs represented by individual configurations: one with flat side chains and flat backbones (Config2 ∼ 60% present), one with tilted side chains and a slightly twisted backbones along the chain (Config3 ∼2% present), and one with tilted side chains and a tilted backbone (Phase I' ∼ 38% present). Backbone "flatness" is defined relative to the top and bottom face of the unit cell. The observed mixture of backbone/side chain tilt angles highlights the large amount of structural heterogeneity in undoped P3HT that makes the determination of atomic scale structure using traditional experiments such as XRD more difficult. The simultaneous occurrence of tilted and flat backbone unit cells reconciles differences in prior experimental studies reporting crystal structures,[15,18,64,67] and makes sense in the context of the formation of nanocrystallites that are known to form in thin films of solution-processed P3HT.[9,33]

P3HT doped with F4TCNQ is dominated by structures with F4TCNQ intercalated between P3HT chains. Here we report a unit cell structure for P3HT with intercalated F4TCNQ that is consistent with INS data, which provides atomic–scale structural information, providing more detail than previous reports which only reported unit cell dimensions. The intercalation of F4TCNQ increases the inter–atomic forces acting on the backbone hydrogen, which causes a blue shift in the OOP bending mode in the INS spectrum. The splitting in the torsional region of the INS spectrum is similar to the splitting displayed by Config2 (Figure 4b), indicating that the presence of F4TCNQ causes the side chains to flatten. The intercalation of F4TCNQ molecules into the crystalline region of P3HT causes the polymer chain to become flatter to best accommodate the packing of a flat dopant molecule. Since each peak is captured by a single configuration, we expect that high doping ratios produce a smaller distribution of local configurations and a more homogeneous film than undoped P3HT, which could impact the electrical properties.

We must emphasize that high-resolution INS contains the information to infer the detailed structural characteristics of disordered systems. However, our ability to model semicrystalline and doped semiconductors polymers is limited by methodology and computational expense. Thus, improved modeling techniques are needed to fully model longer range (lower energy) vibrations over a much larger volume. In particular, modeling techniques that incorporate longer length scales but maintain electronic accuracy are lacking. We anticipate that INS spectroscopy will become a valuable tool in the study of polycrystalline and disordered materials; the structures of countless other disordered materials can be optimized using INS spectroscopy at the VISION instrument.

Supporting Information

Video files of all relevant vibrational modes are present in GIF format.

Acknowledgements

Additional Information

Competing Financial Interests: The Authors declare no competing financial interests.

References

(1) He, Z.; Zhong, C.; Su, S.; Xu, M.; Wu, H.; Cao, Y. Enhanced power-conversion efficiency in polymer solar cells using an inverted device structure. *Nat Photon* **2012**, *6*, 591–595.

(2) Liu, Y.; Zhao, J.; Li, Z.; Mu, C.; Ma, W.; Hu, H.; Jiang, K.; Lin, H.; Ade, H.; Yan, H. Aggregation and morphology control enables multiple cases of high-efficiency polymer solar cells. *Nature communications* **2014**, *5*.

(3) Chen, H.; Guo, Y.; Yu, G.; Zhao, Y.; Zhang, J.; Gao, D.; Liu, H.; Liu, Y. Highly - Extended Copolymers with Diketopyrrolopyrrole Moieties for High-Performance Field-Effect Transistors. *Adv. Mater.* **2012**, *24*, 4618–4622.

(4) Facchetti, A. π-Conjugated Polymers for Organic Electronics and Photovoltaic Cell Applications. *Chem. Mater.* **2011**, *23*, 733–758.

(5) Chen, W.; Xu, T.; He, F.; Wang, W.; Wang, C.; Strzalka, J.; Liu, Y.; Wen, J.; Miller, D. J.; Chen, J.; Hong, K.; Yu, L.; Darling, S. B. Hierarchical Nanomorphologies Promote Exciton Dissociation in Polymer/Fullerene Bulk Heterojunction Solar Cells. *Nano Letters* **2011**, *11*, 3707–3713.

(6) Ko, S. H., Grigoropoulos, C. P., Eds. *Hierarchical Nanostructures for Energy Devices*; RSC Nanoscience & Nanotechnology; The Royal Society of Chemistry, 2015; pp P001–308.

(7) Praprotnik, M.; Site, L. D.; Kremer, K. Multiscale Simulation of Soft Matter: From Scale Bridging to Adaptive Resolution. *Annu. Rev. Phys. Chem.* **2008**, *59*, 545–571.

(8) Glotzer, S. C.; Paul, W. Molecular and mesoscale simulation methods for polymer materials. *Annual Review of Materials Research* **2002**, *32*, 401–436.

(9) Noriega, R.; Rivnay, J.; Vandewal, K.; Koch, F. P. V.; Stingelin, N.; Smith, P.; Toney, M. F.; Salleo, A. A general relationship between disorder, aggregation and charge transport in conjugated polymers. *Nat Mater* **2013**, *12*, 1038–1044.

(10) Venkateshvaran, D. et al. Approaching disorder-free transport in high-mobility conjugated polymers. *Nature* **2014**, *515*, 384–388.

(11) O'Connor, B.; Kline, R. J.; Conrad, B. R.; Richter, L. J.; Gundlach, D.; Toney, M. F.; DeLongchamp, D. M. Anisotropic Structure and Charge Transport in Highly Strain-Aligned Regioregular Poly(3-hexylthiophene). *Advanced Functional Materials* **2011**, *21*, 3697–3705.

(12) Salleo, A.; Kline, R. J.; DeLongchamp, D. M.; Chabinyc, M. L. Microstructural Characterization and Charge Transport in Thin Films of Conjugated Polymers. *Advanced Materials* **2010**, *22*, 3812–3838.

(13) Jimison, L. H.; Toney, M. F.; McCulloch, I.; Heeney, M.; Salleo, A. Charge-Transport Anisotropy Due to Grain Boundaries in Directionally Crystallized Thin Films of Regioregular Poly(3-hexylthiophene). *Advanced Materials* **2009**, *21*, 1568–1572.

(14) Ro, H. W.; Akgun, B.; OConnor, B. T.; Hammond, M.; Kline, R. J.; Snyder, C. R.; Satija, S. K.; Ayzner, A. L.; Toney, M. F.; Soles, C. L.; DeLongchamp, D. M. Poly(3-hexylthiophene) and [6,6]-Phenyl-C61-butyric Acid Methyl Ester Mixing in Organic Solar Cells. *Macromolecules* **2012**, *45*, 6587–6599.

(15) Brinkmann, M.; Rannou, P. Molecular Weight Dependence of Chain Packing and Semicrystalline Structure in Oriented Films of Regioregular Poly(3-hexylthiophene) Revealed by High-Resolution Transmission Electron Microscopy. *Macromolecules* **2009**, *42*, 1125–1130.

(16) Brinkmann, M.; Rannou, P. Effect of molecular weight on the structure and morphology of oriented thin films of regioregular poly(3-hexylthiophene) grown by directional epitaxial solidification. *Advanced Functional Materials* **2007**, *17*, 101–108.

(17) Kline, R. J.; DeLongchamp, D. M.; Fischer, D. A.; Lin, E. K.; Richter, L. J.; Chabinyc, M. L.; Toney, M. F.; Heeney, M.; McCulloch, I. Critical role of side-chain attachment density on the order and device performance of polythiophenes. *Macromolecules* **2007**, *40*, 7960–7965.

(18) Kayunkid, N.; Uttiya, S.; Brinkmann, M. Structural Model of Regioregular Poly(3-hexylthiophene) Obtained by Electron Diffraction Analysis. *Macromolecules* **2010**, *43*, 4961–4967.

(19) Chen, D.; Nakahara, A.; Wei, D.; Nordlund, D.; Russell, T. P. P3HT/PCBM Bulk Heterojunction Organic Photovoltaics: Correlating Efficiency and Morphology. *Nano Letters* **2010**, *11*, 561–567.

(20) Yin, W.; Dadmun, M. A New Model for the Morphology of P3HT/PCBM Organic Photovoltaics from Small-Angle Neutron Scattering: Rivers and Streams. *ACS Nano* **2011**, *5*, 4756–4768.

(21) Kim, Y.; Nelson, J.; Durrant, J. R.; Bradley, D. D. C.; Heo, K.; Park, J.; Kim, H.; McCulloch, I.; Heeney, M.; Ree, M.; Ha, C. S. Polymer chain/nanocrystal ordering in thin films of regioregular poly(3-hexylthiophene) and blends with a soluble fullerene. *Soft Matter* **2007**, *3*, 117–121.

(22) Pacios, R.; Nelson, J.; Bradley, D. D. C.; Virgili, T.; Lanzani, G.; Brabec, C. J. Ultrafast spectroscopic studies in polyfluorene: 6,6 -phenyl C-61-butyric acid methyl ester blend films: monitoring the photoinduced charge transfer process. *Journal of Physics-Condensed Matter* **2004**, *16*, 8105–8116.

(23) Wang, X.; Zhang, D.; Braun, K.; Egelhaaf, H.-J.; Brabec, C. J.; Meixner, A. J. High-Resolution Spectroscopic Mapping of the Chemical Contrast from Nanometer Domains in P3HT:PCBM Organic Blend Films for Solar-Cell Applications. *Advanced Functional Materials* **2010**, *20*, 492–499.

(24) Gao, Y. Q.; Martin, T. P.; Thomas, A. K.; Grey, J. K. Resonance Raman Spectroscopic- and Photocurrent Imaging of Polythiophene/Fullerene Solar Cells. *Journal of Physical Chemistry Letters* **2010**, *1*, 178–182.

(25) Mens, R.; Chambon, S.; Bertho, S.; Reggers, G.; Ruttens, B.; D'Haen, J.; Manca, J.; Carleer, R.; Vanderzande, D.; Adriaensens, P. Description of the nanostructured morphology of [6,6]-phenyl-C61-butyric acid methyl ester (PCBM) by XRD, DSC and solid-state NMR. *Magnetic Resonance in Chemistry* **2011**, *49*, 242–247.

(26) Nieuwendaal, R. C.; Snyder, C. R.; Kline, R. J.; Lin, E. K.; VanderHart, D. L.; DeLongchamp, D. M. Measuring the Extent of Phase Separation in Poly-3-Hexylthiophene/Phenyl-C-61-Butyric Acid Methyl Ester Photovoltaic Blends with H-1 Spin Diffusion NMR Spectroscopy. *Chemistry of Materials* **2010**, *22*, 2930–2936.

(27) DeLongchamp, D. M.; Kline, R. J.; Herzing, A. Nanoscale structure measurements for polymer-fullerene photovoltaics. *Energy & Environmental Science* **2012**, *5*, 5980–5993.

(28) Bavel, S. S. v.; Sourty, E.; With, G. d.; Loos, J. Three-Dimensional Nanoscale Organization of Bulk Heterojunction Polymer Solar Cells. *Nano Letters* **2008**, *9*, 507–513.

(29) van Bavel, S.; Sourty, E.; de With, G.; Veenstra, S.; Loos, J. Three-dimensional nanoscale organization of polymer solar cells. *Journal of Materials Chemistry* **2009**, *19*, 5388–5393.

(30) Chiang, C. K.; Fincher, C. R.; Park, Y. W.; Heeger, A. J.; Shirakawa, H.; Louis, E. J.; Gau, S. C.; Macdiarmid, A. G. Electrical-Conductivity in Doped Polyacetylene. *Physical Review Letters* **1977**, *39*, 1098–1101.

31

(31) Duong, D. T.; Wang, C.; Antono, E.; Toney, M. F.; Salleo, A. The chemical and structural origin of efficient p-type doping in P3HT. *Organic Electronics* **2013**, *14*, 1330–1336.

(32) Pingel, P.; Neher, D. Comprehensive picture of *p*-type doping of P3HT with the molecular acceptor F_4TCNQ. *Phys. Rev. B* **2013**, *87*, 115209.

(33) Jacobs, I. E.; Aasen, E. W.; Oliveira, J. L.; Fonseca, T. N.; Roehling, J. D.; Li, J.; Zhang, G.; Augustine, M. P.; Mascal, M.; Moule, A. J. Comparison of solution-mixed and sequentially processed P3HT:F4TCNQ films: effect of doping-induced aggregation on film morphology. *J. Mater. Chem. C* **2016**, *4*, 3454–3466.

(34) Mitchell, P. C. H.; Parker, S. F.; Ramirez-Cuesta, A. J.; Tomkinson, J. In *Vibrational Spectrocopy with Neutrons*; Finney, J. L., Worcester, D. L., Eds.; Neutron Techniques and Applications; World Scientific, 2005; Vol. 3.

(35) Di Nuzzo, D.; Fontanesi, C.; Jones, R.; Allard, S.; Dumsch, I.; Scherf, U.; von Hauff, E.; Schumacher, S.; Da Como, E. How intermolecular geometrical disorder affects the molecular doping of donor-acceptor copolymers. *Nat Commun* **2015**, *6*, 6460.

(36) Kohn, W.; Sham, L. J. Self-Consistent Equations Including Exchange and Correlation Effects. *Phys. Rev.* **1965**, *140*, A1133–A1138.

(37) Hohenberg, P.; Kohn, W. Inhomogeneous Electron Gas. *Phys. Rev.* **1964**, *136*, B864–B871.

(38) Sauvajol, J. L.; Djurado, D.; Dianoux, A.-J.; Theophilou, N.; Fischer, J. E. Polarized vibrational density of states of polyacetylene from incoherent inelastic neutron scattering. *Phys. Rev. B* **1991**, *43*, 14305–14308.

(39) Sauvajol, J. L.; Djurado, D.; Dianoux, A. J.; Fischer, J. E.; Scherr, E. M.; MacDiarmid, A. G. Polarized vibrational density of states of polyaniline from incoherent

701   neutron scattering: Measurements of the phenyl-ring dynamics. *Phys. Rev. B* **1993**, *47*, 4959–4963.

(40) Papanek, P.; Fischer, J. E.; Sauvajol, J. L.; Dianoux, A. J.; Mao, G.; Winokur, M. J.; Karasz, F. E. Inelastic-neutron-scattering studies of poly(*p* -phenylene vinylene). *Phys. Rev. B* **1994**, *50*, 15668–15677.

(41) Seeger, P. A.; Daemen, L. L.; Larese, J. Z. Resolution of VISION, a crystal-analyzer spectrometer. *Nuclear Instruments and Methods in Physics Research Section A: Accelerators, Spectrometers, Detectors and Associated Equipment* **2009**, *604*, 719 – 728.

(42) Laboratory, O. R. N. Vibrational Spectrometer - VISION. `https://neutrons.ornl.gov/vision`, Accessed: Oct 10, 2016.

(43) Colognesi, D.; Celli, M.; Cilloco, F.; Newport, R.; Parker, S.; Rossi-Albertini, V.; Sacchetti, F.; Tomkinson, J.; Zoppi, M. TOSCA neutron spectrometer: The final configuration. *Applied Physics A* **2002**, *74*, s64–s66.

(44) Jimnez-Ruiz, M.; Ivanov, A.; Fuard, S. LAGRANGE - the new neutron vibrational spectrometer at the ILL. *Journal of Physics: Conference Series* **2014**, *549*, 012004.

(45) Barroso-Bujans, F.; Fernandez-Alonso, F.; Cerveny, S.; Parker, S. F.; Alegria, A.; Colmenero, J. Polymers under extreme two-dimensional confinement: Poly(ethylene oxide) in graphite oxide. *Soft Matter* **2011**, *7*, 7173–7176.

(46) Parker, S. F.; Bowron, D. T.; Imberti, S.; Soper, A. K.; Refson, K.; Lox, E. S.; Lopez, M.; Albers, P. Structure determination of adsorbed hydrogen on a real catalyst. *Chem. Commun.* **2010**, *46*, 2959–2961.

(47) Bousige, C.; Ghimbeu, C. M.; Vix-Guterl, C.; Pomerantz, A. E.; Suleimenova, A.; Vaughan, G.; Garbarino, G.; Feygenson, M.; Wildgruber, C.; Ulm, F.-J.; Pellenq, R.

J. M.; Coasne, B. Realistic molecular model of kerogen/'s nanostructure. *Nat Mater* **2016**, *15*, 576–582.

(48) Hermet, P.; Bantignies, J. L.; Rahmani, A.; Sauvajol, J. L.; Johnson, M. R. Polymorphism of Crystalline α-Quaterthiophene and α-Sexithiophene: Ab Initio Analysis and Comparison with Inelastic Neutron Scattering Response. *The Journal of Physical Chemistry A* **2005**, *109*, 4202–4207.

(49) Yuan, Y.; Zhang, J.; Sun, J.; Hu, J.; Zhang, T.; Duan, Y. Polymorphism and Structural Transition around 54C in Regioregular Poly(3-hexylthiophene) with High Crystallinity As Revealed by Infrared Spectroscopy. *Macromolecules* **2011**, *44*, 9341–9350.

(50) Malik, S.; Nandi, A. K. Crystallization mechanism of regioregular poly(3-alkyl thiophene)s. *Journal of Polymer Science Part B-Polymer Physics* **2002**, *40*, 2073–2085.

(51) Poelking, C.; Andrienko, D. Effect of Polymorphism, Regioregularity and Paracrystallinity on Charge Transport in Poly(3-hexylthiophene) [P3HT] Nanofibers. *Macromolecules* **2013**, *46*, 8941–8956.

(52) Perdew, J. P.; Burke, K.; Ernzerhof, M. Generalized Gradient Approximation Made Simple. *Phys. Rev. Lett.* **1996**, *77*, 3865–3868.

(53) Hamann, D. R.; Schlüter, M.; Chiang, C. Norm-Conserving Pseudopotentials. *Phys. Rev. Lett.* **1979**, *43*, 1494–1497.

(54) Clark, S.; Segall, M.; Pickard, C.; Hasnip, P.; Probert, M.; Refson, K.; Payne, M. First principles methods using CASTEP. *Zeitschrift für Kristallographie* **2005**, 567–570.

(55) Sharifzadeh, S.; Biller, A.; Kronik, L.; Neaton, J. B. Quasiparticle and optical spectroscopy of the organic semiconductors pentacene and PTCDA from first principles. *Phys. Rev. B* **2012**, *85*, 125307.

(56) Jones, J. T. A.; Hasell, T.; Wu, X.; Bacsa, J.; Jelfs, K. E.; Schmidtmann, M.; Chong, S. Y.; Adams, D. J.; Trewin, A.; Schiffman, F.; Cora, F.; Slater, B.; Steiner, A.; Day, G. M.; Cooper, A. I. Modular and predictable assembly of porous organic molecular crystals. *Nature* **2011**, *474*, 367–371.

(57) Ramirez-Cuesta, A. aCLIMAX 4.0.1, The new version of the software for analyzing and interpreting INS spectra. *Computer Physics Communications* **2004**, *157*, 226–238.

(58) Zhu, L.; Kim, E.-G.; Yi, Y.; Brdas, J.-L. Charge Transfer in Molecular Complexes with 2,3,5,6-Tetrafluoro-7,7,8,8-tetracyanoquinodimethane (F4-TCNQ): A Density Functional Theory Study. *Chemistry of Materials* **2011**, *23*, 5149–5159.

(59) Scott, A. P.; Radom, L. Harmonic Vibrational Frequencies: An Evaluation of HartreeFock, MllerPlesset, Quadratic Configuration Interaction, Density Functional Theory, and Semiempirical Scale Factors. *The Journal of Physical Chemistry* **1996**, *100*, 16502–16513.

(60) Lee, C. S.; Dadmun, M. D. Important thermodynamic characteristics of poly(3-hexyl thiophene). *Polymer* **2014**, *55*, 4–7.

(61) Pal, S.; ; Nandi, A. K. Cocrystallization Behavior of Poly(3-alkylthiophenes): Influence of Alkyl Chain Length and Head to Tail Regioregularity. *Macromolecules* **2003**, *36*, 8426–8432.

(62) Snyder, C. R.; Henry, J. S.; DeLongchamp, D. M. Effect of Regioregularity on the Semicrystalline Structure of Poly(3-hexylthiophene). *Macromolecules* **2011**, *44*, 7088–7091.

(63) Adachi, T.; Brazard, J.; Ono, R. J.; Hanson, B.; Traub, M. C.; Wu, Z.-Q.; Li, Z.; Bolinger, J. C.; Ganesan, V.; Bielawski, C. W.; Bout, D. A. V.; Barbara, P. F. Regioregularity and Single Polythiophene Chain Conformation. *Journal of Physical Chemistry Letters* **2011**, *2*, 1400–1404.
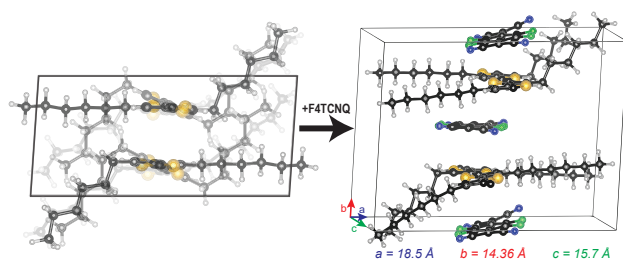
(64) Prosa, T. J.; Winokur, M. J.; Moulton, J.; Smith, P.; Heeger, A. J. X-ray structural studies of poly(3-alkylthiophenes): an example of an inverse comb. *Macromolecules* **1992**, *25*, 4364–4372.

(65) Prosa, T. J.; Winokur, M. J.; McCullough, R. D. Evidence of a Novel Side Chain Structure in Regioregular Poly(3-alkylthiophenes). *Macromolecules* **1996**, *29*, 3654–3656.

(66) Rahimi, K.; Botiz, I.; Stingelin, N.; Kayunkid, N.; Sommer, M.; Koch, F. P. V.; Nguyen, H.; Coulembier, O.; Dubois, P.; Brinkmann, M.; Reiter, G. Controllable Processes for Generating Large Single Crystals of Poly(3-hexylthiophene). *Angewandte Chemie International Edition* **2012**, *51*, 11131–11135.

(67) Dudenko, D.; Kiersnowski, A.; Shu, J.; Pisula, W.; Sebastiani, D.; Spiess, H. W.; Hansen, M. R. A Strategy for Revealing the Packing in Semicrystalline -Conjugated Polymers: Crystal Structure of Bulk Poly-3-hexyl-thiophene (P3HT). *Angewandte Chemie International Edition* **2012**, *51*, 11068–11072.

(68) Shen, X.; Hu, W.; Russell, T. P. Measuring the Degree of Crystallinity in Semicrystalline Regioregular Poly(3-hexylthiophene). *Macromolecules* **2016**, *49*, 4501–4509.

(69) Alexiadis, O.; Mavrantzas, V. G. All-Atom Molecular Dynamics Simulation of Temperature Effects on the Structural, Thermodynamic, and Packing Properties of the Pure Amorphous and Pure Crystalline Phases of Regioregular P3HT. *Macromolecules* **2013**, *46*, 2450–2467.

(70) Li, J.; Zhang, G.; Holm, D. M.; Jacobs, I. E.; Yin, B.; Stroeve, P.; Mascal, M.; Moul, A. J. Introducing Solubility Control for Improved Organic P-Type Dopants. *Chemistry of Materials* **2015**, *27*, 5765–5774.

(71) Segall, M. D.; Pickard, C. J.; Shah, R.; Payne, M. C. Population analysis in plane wave electronic structure calculations. *Molecular Physics* **1996**, *89*, 571–577.

(72) Segall, M. D.; Shah, R.; Pickard, C. J.; Payne, M. C. Population analysis of plane-wave electronic structure calculations of bulk materials. *Phys. Rev. B* **1996**, *54*, 16317–16320.

(73) Salzmann, I.; Heimel, G.; Oehzelt, M.; Winkler, S.; Koch, N. Molecular Electrical Doping of Organic Semiconductors: Fundamental Mechanisms and Emerging Dopant Design Rules. *Accounts of Chemical Research* **2016**, *49*, 370–378, PMID: 26854611.

Table of Contents Graphic

Identifying Atomic Scale Structure in Undoped/Doped Semicrystalline P3HT Using Inelastic Neutron Scattering

Thomas F. Harrelson, Yongqiang Q. Cheng, Jun Li, Ian E. Jacobs, Anibal J. Ramirez-Cuesta, Roland Faller, Adam J. Moulé